Advanced dynamic modeling of three-phase mutually-coupled switched reluctance machine

Dong, Jianning; Howey, Brock; Danen, Benjamin; Lin, Jianing; Weisheng Jiang, James; Bilgin, Berker; Emadi, Ali

DOI
10.1109/TEC.2017.2724765

Publication date
2018

Document Version
Final published version

Published in
IEEE Transactions on Energy Conversion

Advanced Dynamic Modeling of Three-Phase Mutually Coupled Switched Reluctance Machine

Jianning Dong, *Member, IEEE*, Brock Howey, Benjamin Danen, Jianing Lin, *Student Member, IEEE*, James Weisheng Jiang, *Member, IEEE*, Berker Bilgin, *Senior Member, IEEE*, and Ali Emadi, *Fellow, IEEE*

***Abstract*— This paper proposes an advanced dynamic modelling approach of the mutually coupled switched reluctance motor (MCSRM) in the dq reference system that can consider saturation, cross-coupling, and spatial harmonics. Different topologies and their operating principles are investigated and an idealized dq-model considering the inductance harmonics is derived. A dynamic model is built based on flux-current lookup tables (LUTs) obtained from finite element analysis (FEA). A simplified method to inverse the two-dimensional LUTs is proposed. A fast computation approach is used to reduce the number of FEA simulations and calculation time to obtain the LUTs. Motor dynamic performances at different speeds are simulated by using the proposed dynamic model and the results are investigated and verified by FEA. The motor dynamic behavior can be accurately obtained in a short simulation time by using the proposed approach. Experiments are carried out on a 12/8 MCSRM, showing good accuracy of the proposed model.**

***Index Terms*—Dynamic modelling, finite-element method, inductance, mutual coupling, switched reluctance machine.**

I. Introduction

SWITCHED reluctance motors are used in many industries including automotive, textile, aerospace and hand-held power tools due to the obvious merits in terms of robustness, low cost, and reliability. The absence of excitation coils and permanent magnets on the rotor also makes it a good alternative for harsh environments, such as mining. However, the application of conventional switched reluctance machines (CSRM) is also limited by its unconventional power converter, as well as high acoustic noise and vibration levels resulting from its pulsed excitation. These problems can be partially eliminated by using mutually coupled SRMs (MCSRMs), which can be powered with the widely available conventional three-phase inverters [1], [2].

The CSRM uses a decoupled concentrated phase winding so that torque is generated due to the rate of change of the self-inductance of the excitation phase only, which limits the utilization rate of the electrical circuits. The MCSRM operates based on the variation of mutual-inductance between different phases by rewinding the CSRM [3]. Previous research has shown that MCSRM is less sensitive to saturation than the CSRM [4] and has better thermal performance [5]. Multiphysics numerical modeling and experiments also show that the MCSRM has lower vibrations and sound power levels [6]. The torque ripple of the MCSRM is found to be relatively higher, which can be reduced by using a single-layer full-pitched winding [7]. However, its longer end-windings increase the motor volume and deteriorate the rotor stiffness, so concentrated windings are used, as in [1]. The toroidal winding SRM (TWSRM) is proposed as it offers additional winding space, while retaining the benefits of mutual coupling excitation [8], [9].

Dynamic simulation of the CSRM based on offline lookup table (LUT) of phase flux linkage with respect to phase current and rotor position has been extensively used. The LUT can be generated either from finite element analysis (FEA) or experiments. This nonlinear modeling approach is very fast but can provide accurate dynamic waveforms of the CSRM considering electrical circuit switching and magnetic circuit saturation, which is essential for controller design, noise prediction, loss analysis, and hardware-in-loop (HIL) experiments [10], [11]. However, for the MCSRM, the phase flux linkage LUT is extremely complex to produce since the phases are not decoupled anymore. Most of the current literature in this area analyze the dynamic performance of the MCSRM using circuit-coupled time-stepping FEA [6], [12], [13]. This approach can give accurate results, but once the switching and sampling of the digital voltage source inverter (VSI) are considered, the simulation time-step is forced to become very small, resulting in extremely long simulation time that is not suitable for a batched analysis. Decoupling between phases are achieved in [1] by using the dq transformation. However only the static model in the dq reference system is proposed, the dynamic performances are still evaluated directly by FEA; the cross-coupling between the d-axis and q-axis and the inductance spatial harmonics are not discussed.

This paper proposes a dynamic modeling approach based on LUTs, which includes the effects of cross-coupling, saturation,

Manuscript received November 10, 2016; revised April 27, 2017; accepted June 19, 2017. Date of publication July 11, 2017; date of current version February 16, 2018. This work was supported in part by the Canada Excellence Research Chairs Program and in part by the Natural Sciences and Engineering Research Council of Canada (NSERC). Paper no. TEC-00913-2016. *(Corresponding author: J. Dong.)*

J. Dong was with the McMaster Automotive Resource Centre, McMaster University, Hamilton ON L8P 0A6, Canada. He is now with the Delft University of Technology, Delft 2628CD, The Netherlands (e-mail: J.Dong-4@tudelft.nl).

B. Howey, B. Danen, J. Lin, J. W. Jiang, B. Bilgin, and A. Emadi are with the McMaster Automotive Resource Centre, McMaster University, Hamilton, ON L8P 0A6, Canada (e-mail: howeybl@mcmaster.ca; danenbh@mcmaster.ca; linj37@mcmaster.ca; jiangw4@mcmaster.ca; bilginb@mcmaster.ca; emadi@mcmaster.ca).

Color versions of one or more of the figures in this paper are available online at http://ieeexplore.ieee.org.

Digital Object Identifier 10.1109/TEC.2017.2724765

TABLE I
MAIN PARAMETERS OF THE INVESTIGATED SRM

Stator poles	24	Air-gap length [mm]	0.5
Rotor poles	16	Peak power [kW]	60
Stator outer diameter [mm]	264	Peak torque [Nm]	200
Axial length [mm]	92	Base speed [rpm]	2000

and spatial harmonics. A contour line based 2D LUT inversion method and a simplified LUT construction method to reduce the calculation time is proposed. Comparing to the circuit coupling FEA model [6], [12], the proposed model can predict the dynamic current and torque waveforms of the MCSRM accurately with reduced calculation time. The proposed 2D LUT inversion method and the simplified LUT construction method can reduce the model preparation time further. The topologies of the CSRM, MCSRM, and TWSRM and their operating principles are presented in Section II. Then in Section III, the dynamic modeling process, an efficient 2D LUT inversion method and a fast approach to obtain the LUTs is proposed. Section IV compares the dynamic performance of SRMs with different topologies by using the proposed dynamic model. The results are verified by FEA and investigated to show the capabilities of different SRM topologies. In Section V, experiments are carried out on a 12/8 MCSRM prototype. The measured current waveforms are compared with the simulated ones from the dynamic model.

II. MOTOR TOPOLOGIES AND INDUCTANCES

A 24/16 SRM for a hybrid electric vehicle (HEV) application is investigated in this paper. Table I shows the design parameters [14]. The geometry was optimized for CSRM. However, in this paper, the same motor geometry and conductors-per-slot are applied to the CSRM, MCSRM, and TWSRM for validation of the proposed approach. Fig. 1 compares the winding configurations and flux paths when phase A is aligned with the d-axis. The MCSRM is obtained from the CSRM by reversing the polarity of opposite poles [15] while the TWSRM uses the single-layer full-pitch toroidal winding [16]. The maximum phase current for all cases is set at 140 Arms, but the DC bus voltages have been adjusted to ensure that all motors achieve the same 2000 rpm base speed.

Unlike the CSRM, it is apparent that the flux generated by one phase is coupled with the other two phases for both MCSRM and TWSRM configurations in Fig. 1. Obviously, the magnetic motive force (MMF) of the TWSRM is more concentrated than that of the MCSRM, meaning that the TWSRM is more sensitive to saturation.

Fig. 2 shows the self and mutual inductance variations with respect to rotor position, calculated when phase A is supplied with DC current. The self-inductance of the TWSRM is very high but with extremely low ripples, which can be attributed to the compensation effect of different poles. The mutual-inductance is nearly sinusoidal which can lead to lower torque ripple with sinusoidal current excitation. All the inductances change with two cycles during one electrical cycle of the MCSRMs, which means that they contain only even spatial harmonics.

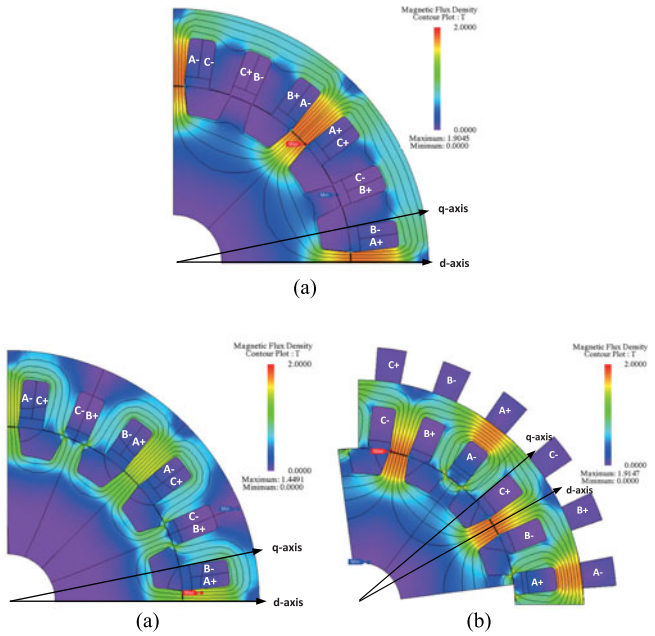

Fig. 1. Flux paths with phase A aligned with d-axis (a) CSRM, (b) MCSRM, (c) TWSRM.

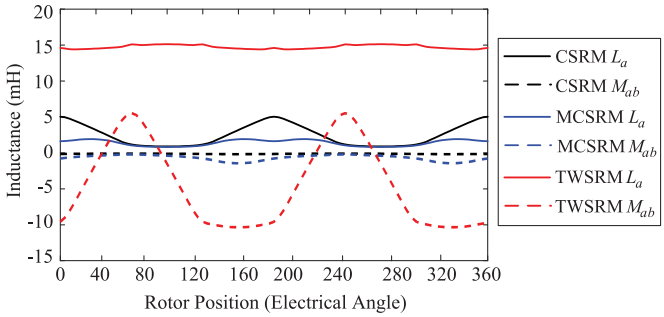

Fig. 2. Self and mutual inductance of CSRM, MCSRM, and TWSRM.

III. DYNAMIC MODEL CONSIDERING SPATIAL HARMONICS

A. DQ-Model of MCSRM and TWSRM

For a symmetric three-phase MCSRM or TWSRM with balanced excitation and without third harmonics, the three-phase state variables (flux linkage ψ, current i, and voltage u) can be converted into the static $\alpha\beta$ reference system by using the Clarke Transformation. If expressed in space vectors, the voltage equation in the $\alpha\beta$ reference system is

$$\boldsymbol{u}_{\alpha\beta} = R_s \boldsymbol{i}_{\alpha\beta} + \frac{d\boldsymbol{\psi}_{\alpha\beta}}{dt} \tag{1}$$

where $\boldsymbol{u}_{\alpha\beta}$, $\boldsymbol{i}_{\alpha\beta}$ and $\boldsymbol{\psi}_{\alpha\beta}$ are space vectors of the voltage, current, and flux linkage in the $\alpha\beta$ reference system respectively. R_s is the phase resistance, and t is time. The relationship between the values in the static $\alpha\beta$ reference system and those in the synchronous rotating dq reference system is

$$\boldsymbol{\psi}_{\alpha\beta} = \boldsymbol{\psi}_{dq} e^{j\theta} \tag{2}$$

where $\boldsymbol{\psi}_{dq}$ is the flux linkage space vector in the dq reference system, θ is the rotor position in electrical angles. If nonlinearity

of the magnetic circuit is neglected for clarity, the flux linkage equation in the static abc reference system is

$$\boldsymbol{\psi}_{abc} = \boldsymbol{L}_{abc}\boldsymbol{i}_{abc} \tag{3}$$

where $\boldsymbol{\psi}_{abc}$ and $\boldsymbol{i}_{abc}$ are the column vector of the three-phase flux linkage and current respectively, $\boldsymbol{L}_{abc}$ is the inductance matrix. As it has been investigated in Section II, $\boldsymbol{L}_{abc}$ of the MCSRM and TWSRM contain only even spatial harmonics:

$$\boldsymbol{L}_{abc} = \sum_{n} \begin{bmatrix} L_n C(n\theta) & M_n Cn\left(\theta + \frac{2\pi}{3}\right) & M_n Cn\left(\theta - \frac{2\pi}{3}\right) \\ M_n Cn\left(\theta + \frac{2\pi}{3}\right) & L_n Cn\left(\theta - \frac{2\pi}{3}\right) & M_n Cn(\theta) \\ M_n Cn\left(\theta - \frac{2\pi}{3}\right) & M_n Cn(\theta) & L_n Cn\left(\theta + \frac{2\pi}{3}\right) \end{bmatrix}$$

$$n = 0, 2, 4, 6, \ldots \tag{4}$$

where C is the cosine function, L_n and M_n are the amplitudes of the n-th harmonics of the self-inductance and mutual-inductance respectively. By applying the amplitude invariant Parks Transformation $\boldsymbol{K}$ to (3) and substituting (4), the flux linkage equation in the dq reference system becomes

$$\begin{aligned} \boldsymbol{\psi}_{dq} &= \boldsymbol{K}\boldsymbol{L}_{abc}\boldsymbol{K}^{-1}\boldsymbol{K}\boldsymbol{i}_{abc} \\ &= \boldsymbol{L}_{dq}\boldsymbol{i}_{dq} \end{aligned} \tag{5}$$

where $\boldsymbol{L}_{dq}$ is the inductance matrix in the dq reference system and is solved as

$$\boldsymbol{L}_{dq} = \sum_{v=0,6,12,\ldots} \begin{bmatrix} L_{dd,v}\cos(v\theta) & L_{dq,v}\sin(v\theta) \\ L_{dq,v}\sin(v\theta) & L_{qq,v}\cos(v\theta) \end{bmatrix} \tag{6}$$

where $L_{dd,v}$, and $L_{qq,v}$ are the amplitudes of the v-th harmonics of the d-axis and q-axis inductances, $L_{dq,v}$ are those of the cross-coupling inductances. We can see that $\boldsymbol{L}_{dq}$ contains spatial harmonics whose orders are multiples of 6 for three phase MCSRM and TWSRM. The electromagnetic torque equation in the dq reference system is

$$T = \frac{3}{2}p\boldsymbol{\psi}_{dq} \times \boldsymbol{i}_{dq} + p\frac{\partial W_{co}}{\partial \theta} \tag{7}$$

where p is the number of rotor pole pairs, W_{co} is the magnetic coenergy [17]. The first term of (7) is labelled as T_{dq} and is produced by the dq axis alignment, while the second term is labelled as T_{co} and is produced by the magnetic coenergy. For the linear case, W_{co} can be computed as

$$W_{co} = \frac{1}{2}\boldsymbol{i}_{dq}^{T}\boldsymbol{L}_{dq}\boldsymbol{i}_{dq} \tag{8}$$

B. Consideration of Saturation Based on LUTs

From (1)–(2) and (5)–(7) we can come up with a dynamic model of the MCSRM. However, even though the spatial harmonics and the cross-coupling are included, the nonlinearity of the magnetic circuit is ignored. When saturation is included, the interpretation of inductances becomes complex since now they depend on both $\boldsymbol{i}_{dq}$ and θ. For calculation considering circuit switching, the incremental inductance makes matters even more complicated [18]. Therefore, the LUT approach which gives the flux-current relationship directly is more commonly used.

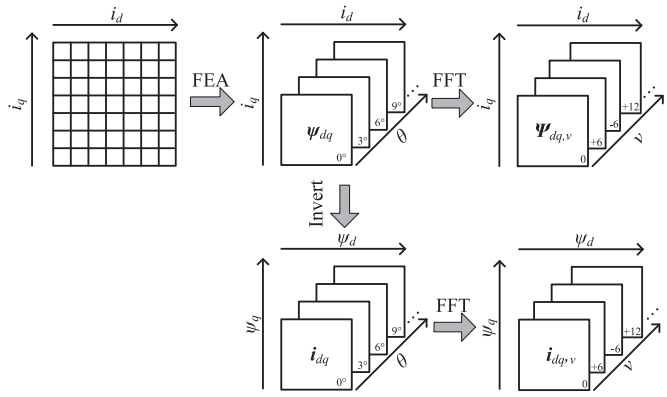

Fig. 3. Procedure to generate the dq LUTs of the flux linkage $\boldsymbol{\psi}_{dq,v}(\boldsymbol{i}_{dq}, \theta)$ and current $\boldsymbol{i}_{dq}(\boldsymbol{\psi}_{dq}, \theta)$.

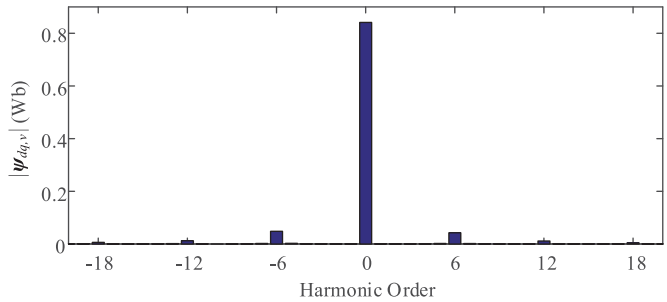

Fig. 4. Spatial harmonic spectrum of $\boldsymbol{\psi}_{dq}(\theta)$.

The upper part of Fig. 3 illustrates the procedure to obtain the flux linkage LUT from FEA. The excitation current pairs are defined as a 2D table in the dq plane. The calculated $\boldsymbol{i}_{dq}$ values are then input into the static FEA model. Both 3D or 2D FEA model can be used. However, for machines with small rotor diameter/length ratio, neglecting of ending effect in 2D models may make significant difference. An estimation of ending leakage will be essential in that case [19].

By evaluating the FEA model along one electrical cycle, the flux linkage $\boldsymbol{\psi}_{dq}$ for each current excitation i_{dq} at each rotor position are solved, composing a 3D table. By using Fast Fourier Transformation (FFT), the amplitude of each spatial harmonic of the flux linkage $\boldsymbol{\psi}_{dq,v}$ is solved and saved as another 3D LUT. Considering only the first 2 harmonics is accurate enough, as shown in Fig. 4. The flux linkage $\boldsymbol{\psi}_{dq}$ for the current excitation $\boldsymbol{i}_{dq}$ is then calculated as

$$\boldsymbol{\psi}_{dq} \approx \sum_{v=0,\pm6,\pm12} \boldsymbol{\psi}_{dq,v}(\boldsymbol{i}_{dq})e^{jv\theta} \tag{9}$$

where the parentheses stand for linear interpolation from the said 3D LUT. The LUT for the coenergy torque T_{co} can also be derived in the same procedure, except that T_{co} is not solved directly from FEA, but obtained by subtracting T_{dq} from T using (7). The dynamic model can be built directly based on the flux linkage LUT $\boldsymbol{\psi}_{dq,v}(\boldsymbol{i}_{dq})$. Then the currents are used as the inputs while the voltages and torque are the outputs. The voltage space vector $\boldsymbol{u}_{\alpha\beta}$ is solved from the derivative of $\boldsymbol{\psi}_{\alpha\beta}$ as is expressed in (1), where $\boldsymbol{\psi}_{\alpha\beta}$ is obtained from (2) and (9). This kind of dynamic model is called an incremental induc-

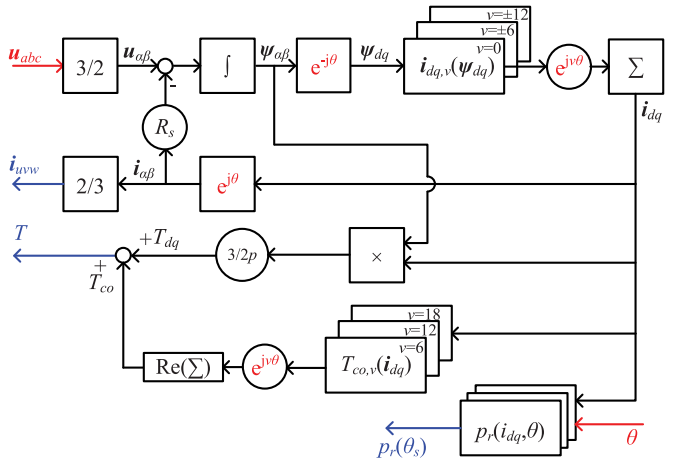

Fig. 5. Dynamic model of the MCSRM based on $\boldsymbol{i}_{dq,v}(\boldsymbol{\psi}_{dq})$.

tance model, which is direct but the differential coefficients in it can amplify errors. Moreover, it is more convenient to use the voltage as inputs when considering the voltage source inverter. Therefore, a dynamic model based on the inverted current LUT $\boldsymbol{i}_{dq,v}(\boldsymbol{\psi}_{dq})$ is proposed here, as is presented in Fig. 5.

The flux linkage-current relationship is inverted at each rotor position and then a FFT is used to obtain the spatial harmonics, as is illustrated in Fig. 3. Now $\boldsymbol{\psi}_{\alpha\beta}$ is obtained from the integral of $\boldsymbol{u}_{\alpha\beta}$, and the current is reconstructed from the linear interpolation of the LUT $\boldsymbol{i}_{dq,v}(\boldsymbol{\psi}_{dq})$

$$\boldsymbol{i}_{dq} \approx \sum_{v=0,\pm6,\pm12} \boldsymbol{i}_{dq,v}(\boldsymbol{\psi}_{dq}) e^{jv\theta} \tag{10}$$

The proposed dynamic model contains only one integrator but no differentiator, which increases the accuracy when compared to the conventional incremental inductance model [10], [18].

C. LUT Inversion

A method based on contour plotting is proposed to invert the LUT. From the original $\boldsymbol{\psi}_{dq}(\boldsymbol{i}_{dq})$ table at a specific rotor position, for each specific flux linkage vector $\boldsymbol{\psi}_{dq}$, we can draw a pair of contour lines for ψ_d and ψ_q respectively. Each of the two contour lines is joint by (i_d, i_q) points which contribute to the same ψ_d or ψ_q value, as shown in Fig. 6. The vertical lines are isolines of ψ_d while the horizontal lines are isolines of ψ_q. The intersection points of the two sets of lines represent the (i_d, i_q) vector which contributes the (ψ_d, ψ_q) vector. For instance, the point B in Fig. 6 indicates that the flux linkage vector $\boldsymbol{\psi}_{dq} = 0.4 - 0.1j$ [Wb] is related to the current vector $\boldsymbol{i}_{dq} = 8.0 - 3.2j$ [A].

MATLAB function *contourc* is used to generate the contour lines of specific ψ_d and ψ_q respectively, which are represented by a group of arrays. Then the intersection point of the two contour lines is obtained by solving linear equations repsenting each line segment.

In this manner, we can map the corresponding points in the dq current plane onto a rectangular grid in the dq flux linkage plane, resulting in a $\boldsymbol{i}_{dq}(\boldsymbol{\psi}_{dq})$ table by determining the intersection points of the contour lines of the $\psi_d(\boldsymbol{i}_{dq})$ table and those of

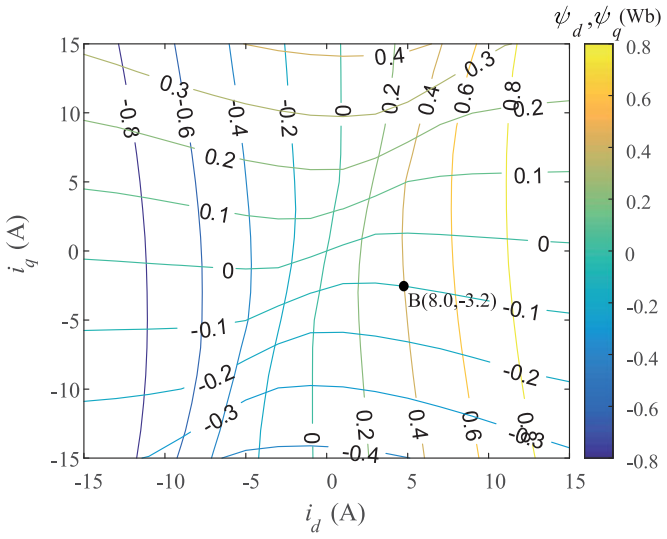

Fig. 6. Isolines of the $\boldsymbol{\psi}_{dq,v}(\boldsymbol{i}_{dq})$ table at $\theta = \pi$.

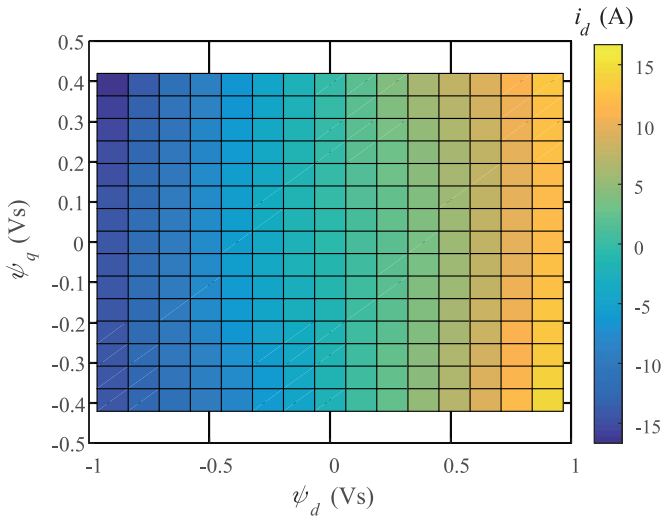

Fig. 7. Contour plot of the inverted $\boldsymbol{i}_d(\boldsymbol{\psi}_{dq})$ table at $\theta = \pi$.

the $\psi_q(\boldsymbol{i}_{dq})$ table. For grid points in the dq flux linkage plane near the boundary, the intersection points for the contour lines of ψ_d and ψ_q may not fall into the rectangular grid range. In this case, their values can be estimated by extrapolation from the neighboring grid points. Fig. 7 presents the contour plot of the inverted $\boldsymbol{i}_d(\boldsymbol{\psi}_{dq})$ table from Fig. 6 using the proposed approach.

D. Fast Computation Approach

As is presented in the last section, a vast number of FEA calculations are needed to obtain the LUTs required by the dynamic model. If we consider only the fundamental and first two harmonics (0, ±6, ±12) for both the i_{dq} LUT and the T_{co} LUT, 60 rotor positions in one electrical cycle for each grid point in the dq current plane is usually a good choice. For a $8 \times 8 i_{dq}$ grid shown in Fig. 4, $4 \times 8 \times 30 = 960$ FEA calculation steps are needed even though the symmetry is used. This paper proposes a fast approach to obtain the essential FEA data with reduced calculation steps. Since we consider only harmonic with order

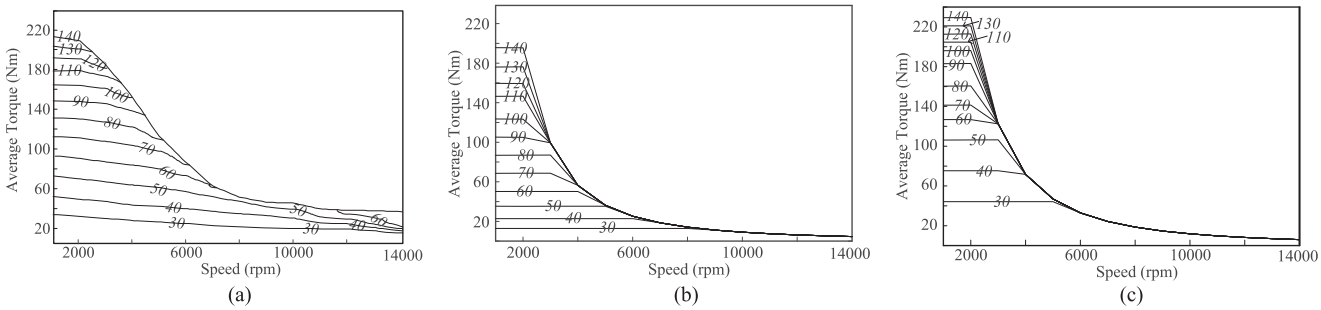

Fig. 8. Torque-speed curve of the motors under different current constraints: (a) CSRM, (b) MCSRM and (c) TWSRM.

0, ± 6 and ± 12, the current vectors at rotor positions of $\theta = 0$, $\pi/12$, $\pi/8$, $\pi/6$ and $\pi/4$ can be expressed by harmonics

$$\boldsymbol{i}_{dq}(\theta_i) = \sum_{v=0,\pm 6,\pm 12} \boldsymbol{i}_{dq,v} e^{jv\theta_i},\ \theta_i \in \left\{0, \frac{\pi}{12}, \frac{\pi}{8}, \frac{\pi}{6}, \frac{\pi}{4}\right\} \quad (11)$$

Then the five harmonics $\boldsymbol{i}_{dq,v}$ can be solved from the five equations in (11) as

$$[\boldsymbol{i}_{dq,v}]_{v=0,\pm 6,\pm 12} = \mathbf{K}_{i2v}\left[\boldsymbol{i}_{dq}(\theta_i)\right] \quad (12)$$

where $\mathbf{K}_{i2v}$ is a 5×5 matrix as expressed in (13) shown at the bottom of this page. The same approach can be applied to the torque results to get the LUT of T_{co} harmonics. By using this fast computation approach, for the same idq grid shown in Fig. 4, only $4 \times 8 \times 5 = 160$ FEA calculation steps are needed to consider the first 2 harmonic orders. Moreover, the computation time of FFT is totally omitted. The overall calculation time to generate the LUTs can be reduced by more than 83%.

IV. Dynamic Simulation and Results Investitation

A. Torque-Speed Characteristics

The torque-speed curve in Fig. 8 for the CSRM are generated with a dynamic model and use multi-objective (maximum average torque and minimum RMS torque ripple) genetic algorithm optimization to determine the firing angles [14], [20]. The MCSRM and TWSRM machines use the maximum torque per ampere (MTPA) excitation angle predicted from the flux LUTs and the torque calculated from (7). All three motors use the same dimensions to validate the proposed approach. The motor geometry was optimized for CSRM. To run MCSRM and TWSRM at the same voltage for the same speed, geometrical modification will be needed. Here DC-link voltages of each SRM type have been adjusted to obtain the same base speed for each machine; 650 V for the CSRM, 850 V for the MCSRM, and 2000 V for the TWSRM. Considering that the TWSRM has roughly double the coil space compared to the other machines, twice the number of turns have been used. The contour labels in Fig. 8 represent the RMS phase current.

Below the base speed, the TWSRM clearly provides the highest average torque, followed by the CSRM, and finally the MCSRM. This is due to the flux-focusing effect of the TWSRM machine, which is reflected by the higher peak flux linkage (see Fig. 11) and the higher torque for a given RMS current (see Fig. 8).

At higher speeds, the CSRM has superior torque output, followed by the TWSRM, and finally the MCSRM. This can be explained by the higher peak current capability for the fixed DC bus voltages. It is important to note that the TWSRM performance at high speeds is expected to be diminished due to the high self-inductances.

In this comparison, the MCSRM performs poorly at both low speeds and high speeds. The self-inductance in the MCSRM is a parasitic effect, as the main torque producing mechanism is dependent on mutual-inductance. Thus, it is expected that the performance of the MCSRM would be more competitive if the geometry were optimized specially for the production of mutual-inductance. This particular geometry appears to be unable to provide significant varying mutual-inductance (see Fig. 2).

B. Transient Results and Validation

The proposed dynamic modelling technique is applied to the MCSRM and TWSRM to simulate the transient current. A 1D LUT based model presented in [14] is used to simulate transient performance of the CSRM. FEA models fed by voltage source waveforms with switching are used to validate the dynamic models. All the three motors are controlled with MTPA control. The hysteresis current controller with the same sampling frequency and relative hysteresis band is used. The reference currents are set at 140 Arms and the rotating speeds are set to 2000 rpm and 10000 rpm respectively. Figs. 9 and 10 compares the transient

$$\mathbf{K}_{i2v} = \frac{1}{8}\begin{bmatrix} 1+(1-\sqrt{2})j & -1+(1+\sqrt{2})j & -4j & 1+(1+\sqrt{2})j & -1+(1-\sqrt{2})j \\ 2 & 2j & 0 & -2 & -2j \\ 2 & 2 & 0 & 2 & 2 \\ 2 & -2j & 0 & -2 & 2j \\ 1+(\sqrt{2}-1)j & -1-(1+\sqrt{2})j & 4j & 1-(1+\sqrt{2})j & -1+(\sqrt{2}-1)j \end{bmatrix} \quad (13)$$

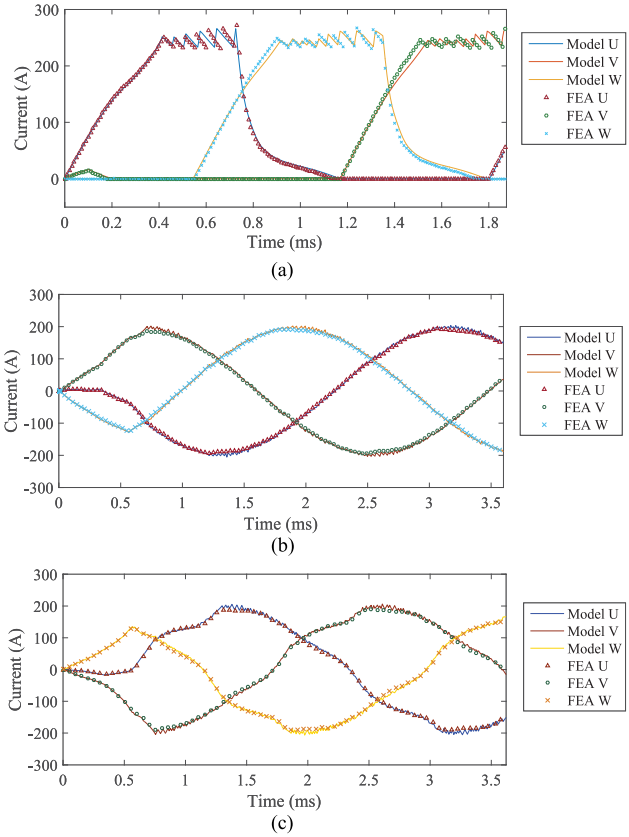

Fig. 9. Current waveforms comparison between dynamic models and FEA at 2000 rpm (a) CSRM, (b) MCSRM and (c) TWSRM.

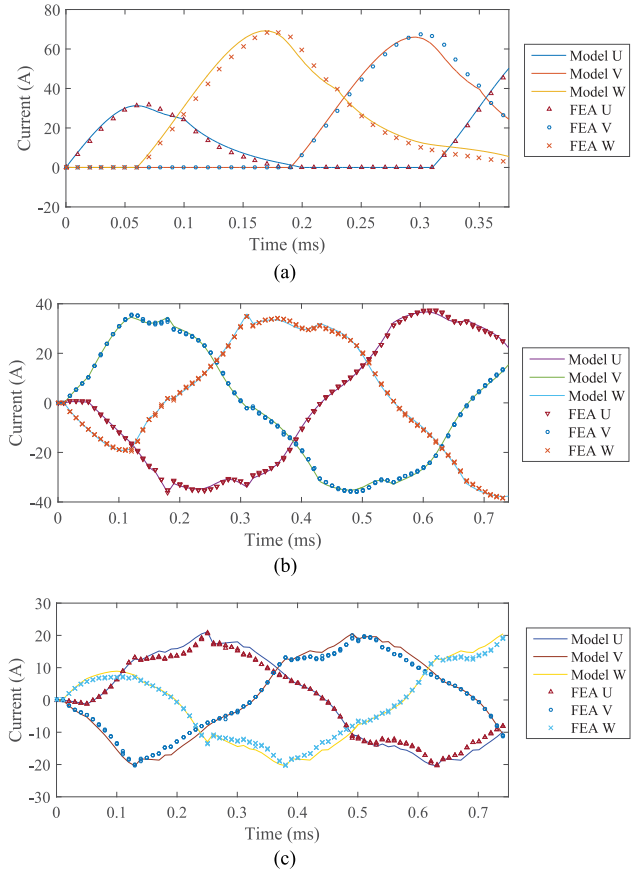

Fig. 10. Current waveforms comparison between dynamic models and FEA at 10000 rpm (a) CSRM, (b) MCSRM and (c) TWSRM.

current waveforms obtained from the proposed dynamic model and those obtained by FEA, illustrating good agreement at both low speed and high speed.

The phase $\psi - i$ curves are plotted from the instantaneous dynamic model phase current and phase flux-linkage at different speeds (labeled as "Phase U" in Fig. 11). The boundary curves (labeled as "Machine Capability" in Fig. 11) are plotted from the flux-linkage LUTs for the CSRM with the maximum RMS current excitation which displays the machines torque capability envelopes.

The flux focusing effect in the TWSRM results in a higher peak flux-linkage and a higher co-energy area. It is clear that the TWSRM is not utilizing the full co-energy area with sinusoidal excitation below the base speed. A different current waveform shape is needed to utilize the co-energy capability more effectively.

The power factor comparison between the three topologies shows that the CSRM clearly has the highest power factor, with 650 V required to obtain the same base speed as the other two designs (requiring 850 V for the MCSRM and 2000 V for the TWSRM, respectively). However, it is not fair to compare these machines by the power factor, as the geometry is optimized for the CSRM.

From Fig. 11 we can see that the CSRM has a moderate co-energy area available for use when compared with the co-energy area of the MCSRM and TWSRM. It is also more saturated than the MCSRM machine when the same current is excited. It is expected that the MCSRM could perform better if the motor is further saturated.

At high speed (5000 rpm), the CSRM has the highest peak flux-linkage per turn, and it also exhibits signs of significant saturation, even at this higher speed. This allows the power factor of the machine to stay at a reasonable value, while the MCSRM cannot maintain this, and the high speed torque and power factor are impacted. However, if the geometry is optimized to properly saturate the MCSRM, it would improve both the power factor and torque output. The TWSRM, with the benefit of flux focusing design, can maintain adequate saturation at higher speeds. However, its higher self-inductance makes it much more sensitive to saturation in the back iron compared to the MCSRM and CSRM [see Fig. 1(c)], and its design must take this into account.

V. Experimental Results and Comparison

The winding of a downscaled 12/8 SRM prototype [21] is modified to the MCSRM configuration to validate the proposed model by experiments. Table II shows the key parameters of the MCSRM prototype.

The shaft of the MCSRM prototype is coupled to a brushless dc (BLDC) machine which works as load. Fig. 12 shows the drive system. The MCSRM works as a motor while the BLDC machine works as a generator. They are driven by the back to back converter. The control scheme is implemented in the DSP

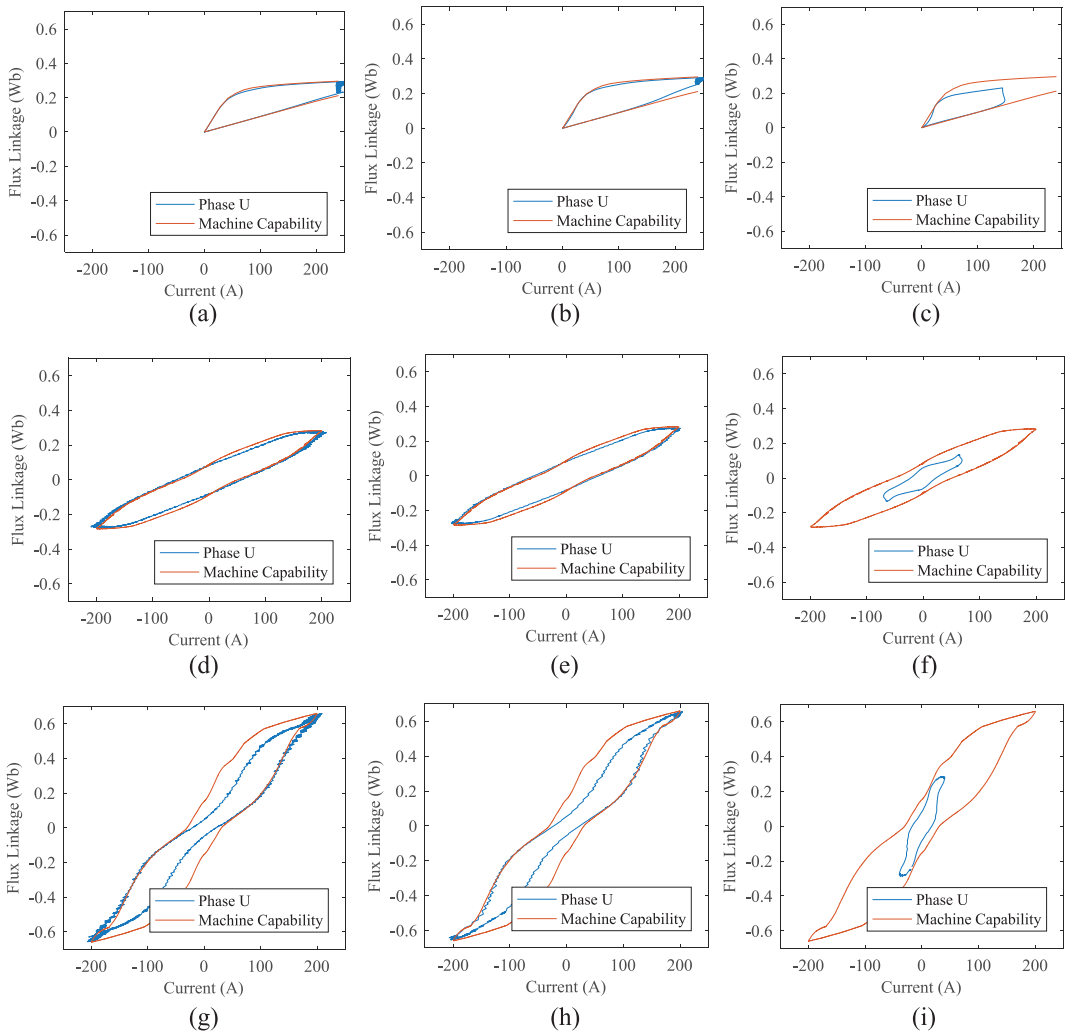

Fig. 11. Phase flux linkage-current curves of each motorat different speeds: (a) CSRM at 1000 rpm (b) CSRM at 2000 rpm (c) CSRM at 5000 rpm. (d) MCSRM at 1000 rpm (e) MCSRM at 2000 rpm (f) MCSRM at 5000 rpm. (g) TWSRM at 1000 rpm (h) TWSRM at 2000 rpm (i) TWSRM at 5000 rpm.

TABLE II
KEY PARAMETERS OF THE 12/8 MCSRM PROTOTYPE

Phase resistance [Ω]	0.44	Rated Torque [Nm]	3.2
Air-gap length [mm]	0.3	Stator outer diameter [mm]	136
Active length [mm]	70	Stator teeth height [mm]	14.9
Rotor teeth height [mm]	11	Stator inner diameter [mm]	83.6

board. Rotor position of the MCSRM is detected by a resolver and fed to the DSP.

The sinusoidal pulse width modulation (SPWM) method is used in the dSPACE controller to generate PWM signals for the inverter. Experiments are carried out with different reference speeds and currents. The same excitation angle, sampling frequency, switching frequency and current controller PI parameters are used in the experimental setup and the dynamic models, as shown in Table III.

Phase current waveforms are measured and saved using an oscilloscope during the experiment. Fig. 13 compares the current waveforms of the MCSRM prototype measured in the experiments and those obtaiend from the dynamic model simulations at 1000 rpm, 10 A and 1500 rpm, 20 A respectively. Apparently,

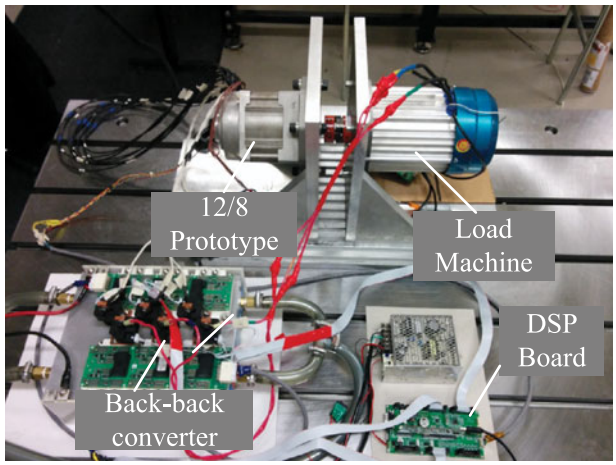

Fig. 12. Experimental setup based on the 12/8 MCSRM prototype.

the simulated waveforms are in close agreement with the experimental ones at both cases. The small deviations between them can be attributed to the neglect of end-winding leakge in the dynamic model and the manufacturing imperfection of the prototype.

TABLE III
PARAMETERS IN THE EXPERIMENTAL DRIVE AND DYNAMIC MODELS

Parameter	Value
DC link voltage	135 V
Reference excitation angle	72.6°
Current sampling frequency	10 kHz
Switching frequency	20 kHz
Current controller parameters	$k_p = 1, k_i = 50$

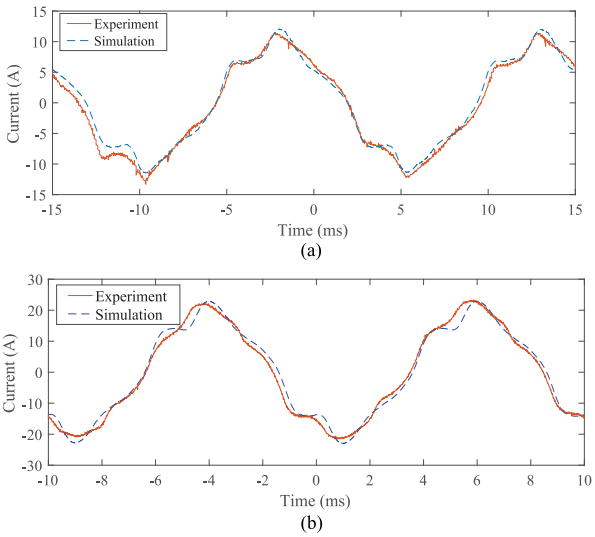

Fig. 13. Comparison between the experimental and simulated phase current waveforms. (a)1000 rpm, 10 A (b) 1500 rpm, 20 A

VI. CONCLUSION

A model for dynamic simulation of the MCSRM based on the current LUTs has been proposed in this paper, which can consider the magnetic nonlinearity, spatial harmonics and switching effects. A method based on contour lines has been raised for the inversion of 2D flux linkage LUTs to current LUTs. A fast computation approach has been proposed to reduce the number of FEA calculations and time to compose the LUTs.

The proposed model has been applied to both a conventional 24/16 MCSRM and a TWSRM for validation based on a geometry which was optimized for CSRM. Their dynamic performances have been calculated using the proposed approach. FEM simulations coupled with voltage source excitations have been involved to validate the results, showing good agreements both for current waveforms and torque waveforms.

Performance of the MCSRM and the TWSRM including torque-speed curves and $\psi - i$ curves under various speeds have been calculated and compared with those of the CSRM using the proposed model. Results have shown that the CSRM generates highest torque at the high speed region while the TWSRM have the highest torque capability at the low speed region, even though the co-energy capability of which is not fully used when excited by sinusoidal current. To fully take the advantages of the MCSRM and the TWSRM, special design criteria which are different from the CSRM should be used.

A drive system based on a 12/8 MCSRM prototype is used for experimental validation of the proposed dynamic model. Experimental results show that the dynamic model can predict the current waveforms accurately.

The works presented in this paper may be used for loss analysis and controller design for the MCSRM and TWSRM. The conclusions give some guidlines for the design of MCSRM and TWSRM.

ACKNOWLEDGEMENT

The authors gratefully acknowledge Powersys Solutions for their support with JMAG software in this research.

REFERENCES

[1] X. Y. Ma, G. J. Li, G. W. Jewell, Z. Q. Zhu, and H. L. Zhan, "Performance comparison of doubly salient reluctance machine topologies supplied by sinewave currents," *IEEE Trans. Ind. Electron.*, vol. 63, no. 7, pp. 4086–4096, Jul. 2016.

[2] E. Bostanci, M. Moallem, A. Parsapour, and B. Fahimi, "Opportunities and challenges of switched reluctance motor drives for electric propulsion: A comparative study," *IEEE Trans. Transp. Electrification*, vol. 3, no. 1, pp. 58–75, Mar. 2017.

[3] B. C. Mecrow, "New winding configurations for doubly salient reluctance machines," *IEEE Trans. Ind. Appl.*, vol. 32, no. 6, pp. 1348–1356, Nov. 1996.

[4] G. Li, J. Ojeda, S. Hlioui, E. Hoang, M. Lecrivain, and M. Gabsi, "Modification in rotor pole geometry of mutually coupled switched reluctance machine for torque ripple mitigating," *IEEE Trans. Magn.*, vol. 48, no. 6, pp. 2025–2034, Jun. 2012.

[5] G. J. Li, J. Ojeda, E. Hoang, M. Lecrivain, and M. Gabsi, "Comparative studies between classical and mutually coupled switched reluctance motors using thermal-electromagnetic analysis for driving cycles," *IEEE Trans. Magn.*, vol. 47, no. 4, pp. 839–847, Apr. 2011.

[6] X. Liang, G. Li, J. Ojeda, M. Gabsi, and Z. Ren, "Comparative study of classical and mutually coupled switched reluctance motors using multiphysics finite-element modeling," *IEEE Trans. Ind. Electron.*, vol. 61, no. 9, pp. 5066–5074, Sep. 2014.

[7] B. C. Mecrow, "Fully pitched-winding switched-reluctance and stepping-motor arrangements," *Proc. Inst. Elect. Eng, Elect. Power Appl.*, vol. 140, pt. C, no. 1, pp. 61–70, Jan. 1993.

[8] R. Marlow, N. Schofield, and A. Emadi, "A continuous toroidal winding SRM with 6- or 12-switch DC converter," *IEEE Trans. Ind. Appl.*, vol. 52, no. 1, pp. 189–198, Jan. 2016.

[9] R. Hoshi, K. Kiyota, A. Chiba, K. Nakamura, and M. Nagano, "Consideration of the winding structure of the toroidal winding switched reluctance motors," in *Proc. 19th Int. Conf. Electr. Mach. Syst.*, 2016, pp. 1–6.

[10] M. Bösing, "Acoustic modeling of electrical drives," Ph.D. dissertation, Dept. Inst. Power Electro. Elect. Drives, RWTH Aachen Univ., Aachen, 2014.

[11] G. Luo, R. Zhang, Z. Chen, W. Tu, S. Zhang, and R. Kennel, "A novel nonlinear modelling method for permanent magnet synchronous motors," *IEEE Trans. Ind. Electron.*, vol. 63, no. 10, pp. 6490–6498, Oct. 2016.

[12] W. Hua, H. Hua, N. Dai, G. Zhao, and M. Cheng, "Comparative study of switched reluctance machines with half-and full-teeth-wound windings," *IEEE Trans. Ind. Electron.*, vol. 63, no. 3, pp. 1414–1424, Mar. 2016.

[13] G. Li, Z. Zhu, X. Ma, and G. Jewell, "Comparative study of torque production in conventional and mutually coupled SRMs using frozen permeability," *IEEE Trans. Magn.*, vol. 52, no. 6, Jun. 2016, Art. no. 8103509.

[14] W. Jiang, "Three-phase 24/16 switched reluctance machine for hybrid electric powertrains: Design and optimization," PhD dissertation, McMaster Univ., McMaster, 2016. [Online]. Available: http://macsphere.mcmaster.ca/handle/11375/19087

[15] J.-W. Ahn, S.-G. Oh, J.-W. Moon, and Y.-M. Hwang, "A three-phase switched reluctance motor with two-phase excitation," *IEEE Trans. Ind. Appl.*, vol. 35, no. 5, pp. 1067–1075, Sep./Oct. 1999.

[16] J. Lin, P. Suntharalingam, N. Schofield, and A. Emadi, "Comparison of high-speed switched reluctance machines with conventional and toroidal windings," in *Proc. 2016 IEEE Transp. Electrification Conf. Expo.*, 2016, pp. 1–7.

[17] N. Bianchi and L. Alberti, "MMF harmonics effect on the embedded FE analytical computation of PM motors," *IEEE Trans. Ind. Appl.*, vol. 46, no. 2, pp. 812–820, Mar. 2010.

[18] J. R. Hendershot and T. J. E. Miller, *Design of Brushless Permanent-Magnet Machines*, 2nd ed. Venice, FL USA: Motor Design Books LLC, Mar. 2010.
[19] A. Matveev, V. Kuzmichev, and E. Lomonova, "A new comprehensive approach to estimation of end-effects in switched reluctance motors," *Proc. Int. Conf. Elect. Mach. , Bruges, Belgium*, 2002, Art. no. 408.
[20] J. W. Jiang, B. Bilgin, B. Howey, and A. Emadi, "Design optimization of switched reluctance machine using genetic algorithm," in *Proc. 2015 IEEE Int. Electr. Mach. Drives Conf.*, May 2015, pp. 1671–1677.
[21] F. Peng, J. Ye, and A. Emadi, "A digital PWM current controller for switched reluctance motor drives," *IEEE Trans. Power Electron.*, vol. 31, no. 10, pp. 7087–7098, Oct. 2016.

Jianning Dong (S'10–M'17) received the B.S. and Ph.D. degrees in electrical engineering from Southeast University, Nanjing, China, in 2010 and 2015, respectively. Since 2016, he has been an Assistant Professor at the Delft University of Technology (TU Delft), Delft, The Netherlands. Before joining TU Delft, he was a post-doc researcher at McMaster Automotive Resource Centre, McMaster University, Hamilton, ON, Canada. His main research interests are design, modelling, and control of electromechanical systems.

Brock Howey received the B.Tech degree in automotive and vehicle technology from McMaster University, Hamilton, ON, Canada, in 2014. During this program he held various co-op positions related to sustainable energy production and vehicle engineering. He is currently working toward the Ph.D degree as part of the Canada Excellence Research Chair in hybrid powertrain program at the McMaster Automotive Resource Center, Hamilton, ON, Canada. He is strongly passionate about vehicles and a firm believer in electric vehicles. His research is currently directed to switched reluctance motor design for vehicle applications.

Benjamin Danen received the B.E. and M.E. degrees in electrical engineering from McMaster University, Hamilton, ON, Canada, in 2014 and 2016, respectively. In September 2014, he joined, as a Research Assistant for the Canada Excellence Research Chair in Hybrid Powertrain Program, McMaster Automotive Resource Centre, Hamilton, ON, Canada, where he is currently a Research Engineer. His research interests include motor control, system modeling, and power electronics.

Jianing Lin (S'13) received the B.Eng. degree in electrical engineering from Southeast University, Nanjing, China, in 2011 and the M.A.Sc. degree in mechanical engineering from McMaster University, Hamilton, ON, Canada, in 2014. She is currently working toward the Ph.D. degree in the Department of Electrical and Computer Engineering, McMaster University. She received the national scholarship in China, as an outstanding graduate receiving several honors in the fields of electrical engineering and business. She has experience in both electrical and mechanical engineering. In 2009, she began her research in electric machines and power electronics. Her main research interests are power electronics, electric machine design, and controller design for applications in electric vehicles and home applications. She is currently focused on high-speed switched reluctance motor designs and control. These designs are suitable for electric bicycles and home applications.

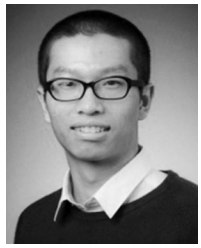

James Weisheng Jiang (S'12–M'16) received the Bachelor' degree in vehicle engineering from the College of Automotive Engineering, Jilin University, Changchun, China, in 2009 and the Ph.D. degree in mechanical engineering from McMaster University, Hamilton, ON, Canada, in April 2016. He was a Research Assistant in the Clean Energy Automotive Engineering Research Center, Tongji University, China, from 2009 to 2011. He is currently a Principal Research Engineer in the Program of the Canada Excellence Research Chair in Hybrid Powertrain at McMaster Automotive Resource Centre, Hamilton, ON, Canada. His main research interests include design of electric vehicle and hybrid electric vehicle powertrains, design of interior permanent magnet motor, design and control of switched reluctance motor, and noise and vibration analysis of traction motors.

Berker Bilgin (S'09–M'12–SM'16) received the Ph.D. degree in electrical engineering from Illinois Institute of Technology, Chicago, Illinois, USA. He is currently working toward the M.B.A. degree in the DeGroote School of Business, McMaster University, Hamilton, ON, Canada. He is the Research Program Manager in Canada Excellence Research Chair in Hybrid Powertrain Program in McMaster Institute for Automotive Research and Technology (MacAUTO), McMaster University. He is managing many multidisciplinary projects on the design of electric machines, power electronics, electric motor drives, and electrified powertrains. He was the General Chair of the 2016 IEEE Transportation Electrification Conference and Expo (ITEC'16).

Ali Emadi (S'98–M'00–SM'03–F'13) received the B.S. and M.S. degrees in electrical engineering with highest distinction from Sharif University of Technology, Tehran, Iran, in 1995 and 1997, respectively, and the Ph.D. degree in electrical engineering from Texas A&M University, College Station, TX, USA, in 2000. He is the Canada Excellence Research Chair in Hybrid Powertrain at McMaster University, Hamilton, ON, Canada. Before joining McMaster University, He was the Harris Perlstein Endowed Chair Professor of Engineering and the Director of the Electric Power and Power Electronics Center and Grainger Laboratories at Illinois Institute of Technology (Illinois Tech), Chicago, IL, USA, where he established research and teaching facilities as well as courses in power electronics, motor drives, and vehicular power systems. He was the Founder, Chairman, and President of Hybrid Electric Vehicle Technologies, Inc.—a university spin-off company of Illinois Tech. He is the principal author/coauthor of more than 400 journal and conference papers as well as several books including *Vehicular Electric Power Systems* (CRC Press, 2003), *Energy Efficient Electric Motors* (CRC Press, 2004), *Uninterruptible Power Supplies and Active Filters* (CRC Press, 2004), *Modern Electric, Hybrid Electric, and Fuel Cell Vehicles* (CRC Press, 2nd ed, 2009), and *Integrated Power Electronic Converters and Digital Control* (CRC Press, 2009). He is also the editor of the *Handbook of Automotive Power Electronics and Motor Drives* (CRC Press, 2005) and *Advanced Electric Drive Vehicles* (CRC Press, 2014). He was the Inaugural General Chair of the 2012 IEEE Transportation Electrification Conference and Expo (ITEC) and has chaired several IEEE and SAE conferences in the areas of vehicle power and propulsion. He is the founding Editor-in-Chief of the IEEE TRANSACTIONS ON TRANSPORTATION ELECTRIFICATION. He has received numerous awards and recognitions. He was the advisor for the Formula Hybrid Teams at Illinois Tech and McMaster University, which won the GM Best Engineered Hybrid System Award at the 2010, 2013, and 2015 competitions.